TSC/mTORC1 mediates mTORC2/AKT1 signaling in c-MYC-induced murine hepatocarcinogenesis via centromere protein M

Yi Zhou[1, 2*], Shu Zhang[3,4*], Guoteng Qiu[5,6], Xue Wang[7], Andrew Yonemura[7], Hongwei Xu[2,5], Guofei Cui[2,7], Shanshan Deng[2,7], Joanne Chun[7], Nianyong Chen[3,4,8], Meng Xu[9], Xinhua Song[10], Jingwen Wang[10], Zijing Xu[10], Youping Deng[7,11], Matthias Evert[12], Diego F. Calvisi[12], Shumei Lin[1], Haichuan Wang[5,6] and Xin Chen[2,7]

[1]Department of Infectious Diseases, the First Affiliated Hospital of Xi'an Jiaotong University, Xi'an, China.

[2] Department of Bioengineering and Therapeutic Sciences and Liver Center, University of California, San Francisco, San Francisco, CA, USA.

[3] Department of Head and Neck Oncology, Cancer Center, West China Hospital, Sichuan University, Chengdu, China.

[4] Department of Radiation Oncology, Cancer Center, West China Hospital, Sichuan University, Chengdu, China.

[5] Division of Liver Surgery, Department of General Surgery, West China Hospital, Sichuan University, Chengdu, China.

[6] Laboratory of Liver Surgery, West China Hospital, Sichuan University, Chengdu, China.

[7] Cancer Biology Program, University of Hawaii Cancer Center, Honolulu, HI, USA.

[8] Laboratory of Single Cell Research and Liquid Biopsy, Cancer Center, West China Hospital, Sichuan University, Chengdu, China.

[9] Department of General Surgery, the Second Affiliated Hospital of Xi'an Jiaotong University, Xi'an, China.

[10]School of Traditional Chinese Medicine, Laboratory for Clinical Medicine, Capital Medical University, Beijing, China.

[11]Department of Quantitative Health Sciences, John A. Burns School of Medicine, Honolulu, Hawaii

[12] Institute of Pathology, University of Regensburg, Regensburg 93053, Germany.

*These authors contributed equally to the work.

Corresponding authors:

Shumei Lin, M.D., Ph.D., Department of Infectious Diseases, the First Affiliated Hospital of Xi'an Jiaotong University, 710061, Xi'an, China. Tel: +86 (029) 85323262. E-mail: lsmxjtu@126.com.

Haichuan Wang, M.D., Division of Liver Surgery, Department of General Surgery, West China Hospital, Sichuan University, 610041, Chengdu, China. Tel: +86 (028) 85422469. E-mail: haichuan.wang@scu.edu.cn.

Xin Chen, Ph.D., Liver Cancer Laboratory, University of Hawaii Cancer Center, 96813, Honolulu, HI, USA. Tel: (808) 564 3804. E-mail: xinchen3@hawaii.edu.

Abstract

Activated mTORC2/AKT signaling plays a role in hepatocellular carcinoma (HCC). Research has shown that TSC/mTORC1 and FOXO1 are distinct downstream effectors of AKT signaling in liver regeneration and metabolism. However, the mechanisms by which these pathways mediate mTORC2/AKT activation in HCC are not yet fully understood. Amplification and activation of c-MYC is a key molecular event in HCC. In this study, we explored the roles of TSC/mTORC1 and FOXO1 as downstream effectors of mTORC2/AKT1 in c-MYC-induced hepatocarcinogenesis. Using various genetic approaches in mice, we found that manipulating the FOXO pathway had minimal impact on c-MYC-induced HCC. In contrast, loss of mTORC2 inhibited c-MYC-induced HCC, an effect that was completely reversed by ablating TSC2, which activated mTORC1. Additionally, we discovered that p70/RPS6 and 4EBP1/eIF4E act downstream of mTORC1, regulating distinct molecular pathways. Notably, the 4EBP1/eIF4E cascade is crucial for cell proliferation and glycolysis in c-MYC-induced HCC. We also identified centromere protein M (CENPM) as a downstream target of the TSC2/mTORC1 pathway in c-MYC-driven hepatocarcinogenesis, and its ablation entirely inhibited c-MYC-dependent HCC formation. Our findings demonstrate that the TSC/mTORC1/CENPM pathway, rather than the FOXO cascade, is the primary signaling pathway regulating c-MYC-driven hepatocarcinogenesis. Targeting CENPM holds therapeutic potential for treating c-MYC-driven HCC.

Keywords: Hepatocellular carcinoma; c-MYC; AKT/mTOR cascade; CENPM; Signal Transduction; Mice Models; Liver Cancer

Introduction

Hepatocellular carcinoma (HCC), the most common type of primary liver cancer, is the second leading cause of cancer death worldwide (1). Several risk factors for HCC development have been identified, including hepatitis B and hepatitis C virus infection, chronic alcohol abuse, and metabolic diseases (2). HCC is amenable to surgery and other potentially curative treatments when diagnosed early. However, effective treatment options for patients with advanced HCC are still limited. Targeted therapy with multi-targeted kinase inhibitors such as sorafenib did not result in a reasonable survival benefit (3, 4), probably due to the activation of alternative pathways leading to treatment evasion. Recently, immune checkpoint inhibitor-based immunotherapy has become the first-line treatment for advanced HCC. However, a notable portion of HCC patients do not respond to this therapy (5, 6). Thus, there is an urgent need to investigate the molecular mechanisms leading to HCC development and progression to develop novel therapies against HCC.

Activated v-akt murine thymoma viral oncogene homolog (AKT) /mammalian target of rapamycin (mTOR) signaling plays a pivotal role in human hepatocarcinogenesis (7). mTOR consists of two functionally distinct protein complexes: mTORC1 and mTORC2, which are distinguished by two unique accessory proteins, the regulatory-associated protein of mTOR (RAPTOR) and the rapamycin-insensitive companion of mTOR (RICTOR). RAPTOR and RICTOR define mTORC1 and mTORC2, respectively (8, 9). mTORC1 promotes protein synthesis by phosphorylating two downstream effectors, eukaryotic translation initiation factor 4E-binding protein 1 (4EBP1) and ribosomal protein S6 kinase 1 (S6K1), whereas mTORC2 phosphorylates AKT at the Ser473 site. Once activated, AKT induces mTORC1 by inhibiting its negative regulators TSC1/2. In addition, AKT phosphorylates forkhead box O (FOXO) transcription factors, especially FOXO1, leading to cell growth, survival, and proliferation. Previous studies have revealed distinct TSC/mTORC1 and

FOXO1 functions as downstream effectors of AKT signaling in liver regeneration and metabolism (10-12). For example, in liver regeneration, it has been shown that FOXO1 is the major downstream effector downstream of AKT (11). FOXO1 is also the key molecule regulating AKT-mediated insulin response in the liver (13). However, how these cascades mediate mTORC2/AKT activation in HCC remains to be defined.

As a well-characterized oncogene, c-MYC activation is a critical genetic event in human HCC. Deregulated c-MYC expression triggers selective gene expression responsible for cell growth, proliferation, metabolism, and tumorigenesis (14). The investigation of the biochemical crosstalk between c-MYC and mTOR pathways during tumor development has shown that mTORC2/AKT1 is required for c-MYC-driven HCC. Specifically, Rictor (mTORC2) or Akt1 ablation inhibits c-MYC HCC formation in mice (15, 16). In the present study, we characterized the functional role of the major downstream effectors of AKT in c-MYC-driven hepatocarcinogenesis. We discovered that TSC/mTORC1, but not the FOXO cascade, is the pivotal signaling pathway regulating c-MYC-driven HCC development. Mechanistically, we identified the centromere protein M (CENPM) as a critical downstream target of the TSC2/mTORC1 pathway in c-MYC HCC.

Results

Deletion of *Foxo1* fails to rescue the loss of *Rictor*'s tumor inhibition effects in c-MYC HCC

Our previous study demonstrated that c-MYC-driven HCC is mTORC2/AKT1 dependent. Indeed, ablation of *Rictor* or *Akt1* completely suppresses c-MYC-induced HCC formation in the mouse (15). As the first step to investigate the pathways regulated by mTORC2/AKT, we tested the hypothesis that FOXO1 is a transcription factor downstream of mTORC2/AKT1 in murine c-MYC HCC formation. Thus, we analyzed the activation status of FOXO1 in the mouse c-MYC HCC. While strong nuclear immunoreactivity for total and phosphorylated/inactivated FOXO1

characterized the tumor compartment and the adjacent non-tumorous surrounding liver tissues, only the tumor lesions displayed robust cytoplasmic immunolabeling for the two proteins (Supplementary Fig. 1A). In addition, Western blot analysis demonstrated increased levels of phosphorylated FOXO1 in the mouse c-MYC tumors (Supplementary Fig. 1B). Moreover, microarray analysis of mouse c-MYC HCC (17) revealed that expression of FOXO1 downstream genes were suppressed (Supplementary Fig. 1C). Overall, these data indicate that FOXO1 signaling is inactivated in c-MYC HCC.

We reasoned that if FOXO1 is the major effector, ablation of *Foxo1* will rescue the loss of *Rictor*'s tumor growth inhibitory effects. While c-MYC could not induce HCC formation in the *Rictor* knockout (KO) genetic background, c-MYC could drive HCC development in *Foxo1;Rictor* double KO background if our hypothesis is correct. Thus, we generated $Rictor^{fl/fl};Foxo1^{fl/fl}$ mice in the *C57BL/6J* background. As c-MYC alone cannot induce HCC in the *C57BL/6J* genetic background, we co-injected the MCL1 oncogene in these mice, as reported before (17). In brief, $Rictor^{fl/fl};Foxo1^{fl/fl}$ mice were co-injected with c-MYC, MCL1, and Cre plasmids, allowing the expression of c-MYC/MCL1 in *Rictor;Foxo1* double KO hepatocytes (c-MYC/MCL1/Cre). Additional $Rictor^{fl/fl};Foxo1^{fl/fl}$ mice were co-injected with c-MYC, MCL1, and pCMV empty vector as controls (c-MYC/MCL1/pCMV) (Figure 1A). None of the c-MYC/MCL1/Cre injected $Rictor^{fl/fl};Foxo1^{fl/fl}$ mice developed liver tumor even at 20 weeks post-injection, while all c-MYC/MCL1/pCMV injected mice developed a lethal tumor burden and required euthanasia between 4-8 weeks post-injection (Figure 1B and 1C). The c-MYC/MCL1/Cre mouse livers appeared completely normal in gross and histological images. In contrast, poorly differentiated and highly proliferative HCC lesions were observed throughout the liver of the control group (Figure 1D). The phenotype recapitulated what we observed when c-MYC/MCL1/Cre plasmids

were injected into *Rictor*$^{fl/fl}$ mice. The results indicate that deleting *Foxo1* fails to rescue the loss of mTORC2's tumor inhibitory effects.

Overexpression of a constitutively actived FOXO1 or FOXO3 does not affect c-MYC-driven liver tumorigenesis *in vivo*

As there are multiple FOXO family isoforms and FOXO3/4 were also inactivated in the c-MYC tumors (Supplementary Fig. 1A and 1B), we could not exclude that other FOXOs compensate for the loss of *Foxo1* tumor suppressor in the double KO studies. Therefore, we overexpressed the c-MYC oncogene with a MYC-tagged constitutively active form of FOXO1 (FOXO1AAA)Due to the common DNA binding motifs of FOXO family members, it has been suggested that FOXO1AAA activates genes that are regulated by other FOXO members (18, 19). Additional mice were injected with c-MYC and pT3-EF1α empty vector as the control (Figure 2A). Consistent with the results from the *Foxo1;Rictor* double KO studies, both c-MYC/FOXO1AAA and c-MYC/pT3-EF1α mice developed high tumor burden and had to be euthanized by 6 to 9 weeks post-injection, suggesting that activated FoxO1 does not improve the survival of c-MYC mice (Figure 2B). There was no significant difference in tumor burden, as revealed by liver weight between c-MYC/FOXO1AAA and c-MYC/ pT3-EF1α cohorts (Figure 2C). Gross images and histological analysis showed that c-MYC/FOXO1AAA mice had a similar tumor burden and histology to the control group. The staining for MYC-tag confirmed the overexpression of FOXO1AAA in c-MYC/FOXO1AAA HCC (Figure 2D). Western blot analysis also confirmed the expression of FOXO1AAA and c-MYC in liver tumors. Additional downstream components of AKT and mTORC1 signaling (TSC2， p-PRS6, and p-4E-BP1) did not differ in protein levels between c-MYC/FOXO1AAA mouse liver tissues and controls. The expression of p-AKT^{S473} increased after FOXO1 activation, indicating the feedback activation of the mTORC2 pathway (Supplementary Fig. 2A). To further strengthen our findings, we overexpressed the constitutively active form of

FOXO3 (FOXO3AAA), which is known to regulate the cell death and cell cycle in the liver (20), together with c-MYC (Supplementary Fig. 3A). Consistently, FOXO3AAA also had limited effect on the development of c-MYC tumors (Supplementary Fig. 3). Overall, the data show that overexpressing activated FOXOs does not inhibit liver tumor development in c-MYC mice, suggesting a limited role of the FOXO pathway in c-MYC dependent hepatocarcinogenesis.

While FOXO proteins may possess limited roles in promoting or delaying c-MYC driven HCC formation, they might still function by modulating molecular features of the tumor cells. To test this hypothesis, we performed RNA-seq analysis on the c-MYC/FOXO1AAA and c-MYC/pT3 tumors as well as the wildtype (WT) normal liver tissues. We found that known FOXO1 target genes were constantly upregulated in c-MYC/FOXO1AAA mouse HCC when compared to c-MYC/pT3 tumors (Supplementary Fig. 2B), confirming the reliability of the RNASeq studies. Further analysis revealed the distinct gene expression patterns of c-MYC/FOXO1AAA and c-MYC/pT3 HCCs (Supplementary Fig. 4). Specifically, we identified 735 genes upregulated in c-MYC/pT3 group compared to the normal liver, but their expression were downregulated by FOXO1AAA expression (Supplementary Fig. 5A, C; Supplementary Table1). In addition, 1206 genes were downregulated in c-MYC/pT3 mouse HCC when compared to the normal liver tissues, but were upregulated by FOXO1AAA expression (Supplementary Fig. 5B, D; Supplementary Table1). Intriguingly, many of these genes were related to various metabolic pathways (Supplementary Fig. 5), suggesting that FOXO proteins might be critical regulators of HCC metabolism. Thus, the genomic analyses strongly suggest that while FOXO1AAA might not affect c-MYC cancer development *per se*, but it could modify the gene expression patterns, especially metabolic pathways, of the tumor.

TSC/mTORC1 is the major downstream effector of AKT along c-MYC-driven hepatocarcinogenesis

TSC2 is directly phosphorylated and inactivated by AKT, which results in mTORC1 activation (21, 22). Hence, the ablation of *Tsc2* would lead to persistent activation of the mTORC1 signaling pathway. Our previous study revealed the mTORC1 pathway was activated and required for c-MYC-induced HCC initiation (16). Here, we aimed to determine whether TSC/mTORC1 is the major downstream effector of AKT along c-MYC-dependent HCC formation. To test this hypothesis, we asked whether loss of *Tsc2* is sufficient to rescue loss of *Rictor's* tumor inhibitor effects. We generated $Rictor^{fl/fl}Tsc2^{fl/fl}$ double conditional KO mice. Subsequently, c-MYC, MCL1, and pCMV-Cre or pCMV plasmids were injected into the mice (Figure 3A). We discovered that c-MYC/MCL1/Cre injected $Rictor^{fl/fl}Tsc2^{fl/fl}$ mice induced lethal tumor burden within 1.7-4.0 weeks post-injection, while in control mice fatal tumor burden occurred at 4.1-8.7 weeks post-injection (Figure 3B). Deletion of *Rictor/Tsc2* also resulted in an increased tumor burden as shown in liver weight compared to the control group (Figure 3C). At the molecular level, Western blot analysis demonstrated that Rictor and TSC2 were successfully knocked out in Cre injected mouse liver tissues. Also, $p\text{-}AKT^{S473}$ levels were decreased, supporting the inactivation of mTORC2. The downstream effectors of mTORC1, including p-RPS6 and p-4EBP1, were expressed at higher levels, supporting the activation of mTORC1 (Figure 3D). Higher proliferation rates were detected throughout the liver of c-MYC/MCL1/Cre mice, as revealed by Ki67 staining (Figure 3E). The results indicate that the deletion of *Tsc2* fully rescues c-MYC-driven hepatocarcinogenesis in *Rictor*-deficient mice.

The findings above suggest that loss of TSC1 or TSC2 may accelerate c-MYC-driven HCC development. Thus, we investigated whether such phenotypes could be observed in human HCC samples. We retrieved the Cancer Genome Atlas-Liver Hepatocellular Carcinoma (TCGA-LIHC)

dataset (23) and analyzed the correlation between the c-MYC activation status and *TSC1/2* mutation status in human HCC. To reflect c-MYC activation status, 30 well-known downstream target genes of c-MYC were used as the c-MYC activation signature (Supplementary Fig. 6A). We found that 52.4% of *TSC1/2* mutant HCC samples had activated c-MYC status. In contrast, 26.1% of wild-type samples showed c-MYC activation (Supplementary Fig. 6B). HCCs with high c-MYC activation displayed significantly higher *TSC1/2* mutation rate, suggesting the important role of TSC/mTORC1 during c-MYC tumor development.

Next, we further determined whether the ablation of *Tsc2* alone could also accelerate c-MYC tumor development without MCL1. Thus, we co-expressed c-MYC/Cre or pCMV into $Tsc2^{fl/fl}$ mice (in the *FVB/N* background) (Supplementary Fig. 7A). The c-MYC/pCMV injected mice developed a lethal tumor burden and were euthanized within 8.9 to 13.0 weeks post-injection. In comparison to the control mice, all c-MYC/Cre injected mice developed a lethal burden of liver tumors within 3.4 to 6.0 weeks post-injection (Supplementary Fig. 7B). The c-MYC/Cre mice displayed a higher tumor burden than c-MYC/pCMV control mice (Supplementary Fig. 7C). Loss of TSC2 protein was confirmed by Western blot analysis. High expression of phosphorylated RPS6, the downstream effector of mTORC1, as well as increased expression of cleaved caspase 3, was detected in liver tissues from c-MYC/Cre injected $Tsc2^{fl/fl}$ mice (Supplementary Fig. 7D). No histopathological alterations were detected in liver sections of c-MYC/Cre injected mice and control mice (Supplementary Fig. 7E).

Our previous study suggests that mTORC1 is necessary for c-MYC-driven HCC initiation (16). We also investigate whether mTORC1 is required for the progression of c-MYC HCC. For this purpose, we used a tamoxifen-inducible CreERT2 system to create a conditional *Raptor* KO mouse HCC model. We utilized a transposase-based vector, pT3-TTR-CreERT2, which

incorporates the TTR-CreERT2 transgene under the control of hepatocyte-specific transthyretin (TTR) promoter. We co-expressed c-MYC, MCL1, and pT3-TTR-CreERT2 into *Raptor*$^{fl/fl}$ mouse liver by hydrodynamic injection. Two weeks post-injection, tumor nodules were observed, and the tumor-bearing mice were subsequently treated with tamoxifen or a vehicle via intraperitoneal injection (Supplementary Fig. 8). Tamoxifen treatment activated Cre recombinase and deleted Raptor in tumor cells, allowing us to investigate the role of mTORC1 in the already formed HCCs. Tamoxifen treatment significantly improved the overall survival rate (Supplementary Fig. 9). Interestingly, large areas of necrosis were frequently observed in tamoxifen-treated livers (Supplementary Fig. 10). By the end of observation, the tamoxifen-treated group only developed 3 small individual tumor nodules in this mouse cohort. IHC revealed the expression of RAPTOR protein in all the tumor nodules (Supplementary Fig. 11). Since we have previously proved the efficiency of the TTR-Cre-ERT2 system (24), we reasoned that such tumor nodules were escapers. These findings prove that *Raptor* ablation in tumor cells induces significant liver tumor regression in c-MYC mice.

In summary, the mouse and human studies suggest that TSC/mTORC1 is the main effector downstream of mTORC2/AKT1 in c-MYC-driven HCC, and loss of TSC accelerates c-MYC-induced liver tumor formation.

p70S6K/RPS6 and 4EBP1/eIF4E cascades regulate distinct pathways during c-MYC tumorigenesis

According to our previous research, both the p70S6K/RPS6 and 4EBP1/eIF4E cascades operate downstream of mTORC1 in HCC (25). These findings were further corroborated in c-MYC/MCL1/*Rictor*^{KO}*Tsc2*^{KO} liver tumor lesions induced with c-MYC/MCL1/Cre in *Rictor*$^{fl/fl}$*Tsc2*$^{fl/fl}$ mice. We observed that the inhibition of p70S6K/RPS6 using everolimus or the use of 4EBP1A4,

the unphosphorylatable form of 4EBP1, blocked tumor development in these mice (Supplementary Figs. 12 and 13). Subsequently, we investigated the pathways regulated by p70S6K/RPS6 and 4EBP1/eIF4E cascades in c-MYC-driven HCC. However, we discovered that tumors still developed in mice overexpressing 4EBP1A4 (Supplementary Fig. 14), likely due to compensatory mechanisms that led to the resistance to 4EBP1/eIF4E pathway inhibition over the long-term course of tumor growth. Consequently, we pursued an alternative approach. We treated *c-MYC/MCL1/Rictor*^{KO}*Tsc2*^{KO} HCCs with MLN0128 (Figure 4A). MLN0128 is a pan-mTOR inhibitor that suppresses both mTORC1 and mTORC2. In *c-MYC/MCL1/Rictor*^{KO}*Tsc2*^{KO} mouse tumors, where *Rictor* is lost, mTORC2 is effectively inactivated, making MLN0128 the ideal inhibitor of mTORC1, including both the p70S6K/RPS6 and 4EBP1/eIF4E pathways. Indeed, we found that MLN0128 treatment effectively suppressed *c-MYC/MCL1/Rictor*^{KO}*Tsc2*^{KO} tumor growth, and it was more effective than the p70S6K/RPS6 inhibitor everolimus (Figure 4).

To identify the gene expression patterns regulated by the p70S6K/RPS6 and 4EBP1/eIF4E cascades, we treated *c-MYC/MCL1/Rictor*^{KO}*Tsc2*^{KO} mouse HCCs with everolimus (to inhibit p70S6K/RPS6) or MLN0128 (to inhibit both p70S6K/RPS6 and 4EBP1/eIF4E) for three days (Figure 5A). RNASeq experiments were performed. Normal liver tissues and vehicle-treated tumors were used as the controls. We focused on genes upregulated in mouse HCC samples and downregulated by everolimus and/or MLN0128. Specifically, 5367 genes were upregulated (fold change, >1.5; *P* adj < 0.05) in tumor tissues compared with normal livers. Among them, 625 genes were downregulated upon everolimus and MLN0128 treatment, implying that these genes are presumably downstream molecules regulated by the p70S6K/RPS6 pathway. In addition, 565 genes were downregulated by MLN0128 but not by everolimus, indicating that these genes are likely regulated by the 4EBP1/eIF4E cascade (Figure 5A).

KEGG enrichment analysis revealed that p70S6K/RPS6 or 4EBP1/eIF4E regulated different biological processes (Figure 5B and 5C). It has been previously established that p70S6K/RPS6 is a pivotal regulator of tumor cell metabolism (26). On the other hand, the genes or pathways regulated by 4EBP1/eIF4E are not well defined. Therefore, we focused on analyzing the differentially down-regulated genes affected by MLN0128 treatment only, i.e., 4EBP1/eIF4E pathway genes. These genes were enriched in the cell cycle and metabolic pathways required for cell proliferation, including glycolysis, citrate cycle, and carbon metabolism (Figure 5D and Supplementary Fig. 9A). Western blot analysis confirmed the decreased expression of glycolysis-related proteins, LDHA/C and PKM1, in MLN0128 treated tumors (Supplementary Fig. 9B).

As a primary downstream target of mTORC1 signaling, the 4EBP1/eIF4E cascade promotes c-MYC-driven HCC development by regulating tumor cell proliferation.

CENPM is the pivotal target gene downstream of mTORC1 in c-MYC HCC

Next, we searched for potential downstream effectors of the mTORC1 cascade, especially those downstream of the 4EBP1/eIF4E pathway, in c-MYC-induced liver lesions. We identified the genes upregulated in tumor tissues and downregulated by MLN0128 treatment but not by everolimus treatment (based on RNAseq data). Among them, 30 genes were also overexpressed in c-MYC mouse liver tumors based on our previous microarray analysis data (16). Each gene was searched in the TCGA-LIHC dataset for any possible link to HCC. Four genes were upregulated in human HCCs and are associated with poor prognosis of the patients: ARHEGF2, BAT1, CENPM, and SLC7A11 (Figure 6A). Subsequently, we analyzed their expression in human HCC cell lines upon Everolimus or MLN0128 treatment. Of note, only CENPM was consistently downregulated by MLN0128 (Figure 6B and Supplementary Fig. 15A). Western blot results showed that everolimus only inhibited the activation of RPS6 signaling, while MLN0128, a pan-

mTOR inhibitor, inhibited both RPS6 and 4EBP1 pathways downstream of mTORC1 (Figure 6C). These results suggested that CENPM is a 4EBP1/eIF4E target downstream of mTORC1. CENPM is one of the critical components of a complex that allows kinetochore protein assembly, mitotic progression, and chromosome segregation. In the TCGA database, CENPM mRNA expression was significantly upregulated in human HCC tissues compared to surrounding tissues (Figure 6D). In addition, low expression levels of CENPM were linked to a better prognosis in human HCC cohorts (Figure 6E). CENPM expression was also positively correlated with EIF4EBP1, the major downstream effector of mTORC1 (Figure 6F). In addition, we also found that CENPM levels positively correlated with levels of MYC activation (Supplementary Fig. 15B). Thus, we hypothesized that CENPM might be a candidate target gene downstream of mTORC1/4EBP1 in c-MYC-induced HCC.

To investigate the role of CENPM in c-MYC HCC progression, we infected 2 HCC cell lines (HLF and Huh7) with 4-hydroxytamoxifen (4OHT)-inducible c-MYC lentivirus (p-Lenti-4OHT-cMyc-ER). As our previous studies revealed (15, 16), c-MYC is expressed at low levels in HLF and Huh7 cell lines. Upon 4OHT treatment, c-MYC expression was induced, and the CENPM mRNA levels were concomitantly upregulated in HLF and Huh7 cells (Figure 6G).

To further characterize the effect of CENPM in c-MYC HCC tumor development, we silenced CENPM in human HCC cell lines using small interfering RNA (siRNA; siCENPM). The cell viability was strongly inhibited by siCENPM, as revealed by EdU staining (Supplementary Fig. 16). Consistently, based on DEPMAP studies, sgRNA against CENPM also led to significant HCC cell growth inhibition in all 22 human HCC cells tested (Supplementary Fig. 17). To validate this observation, two human HCC cell lines, HLF and Hep40, were also transfected with sgCENPM (human) lentivirus. Of note, the human HCC cell proliferation was significantly inhibited, as EdU

and colony formation assays showed. In addition, CENPM protein expression was remarkably reduced (Figure 7A-E). Moreover, immunofluorescence-based microscopy analysis of CENPM KO single cells suggested the influence of this gene on chromosome segregation in HCC cells. Specifically, lagging chromosomes or mis-segregations were observed in the CENPM KO cells during mitosis, likely due to abnormal kinetochores proteins caused by CENPM loss (Figure 7F and Supplementary Fig. 18).

Next, to investigate the role of CENPM in c-MYC-induced hepatocarcinogenesis *in vivo*, we co-expressed c-MYC, MCL1, and CRISPR-Cas9 mediated knockout plasmid (sgCenpm) in mouse liver by hydrodynamic injection, while c-MYC, MCL1, and sgEGFP plasmids were injected into additional mice as controls (Figure 7G). Strikingly, *Cenpm* deletion completely suppressed c-MYC HCC formation in mice (Figure 7H and I). Indeed, twenty weeks post-injection, none of the c-MYC/ MCL1/sgCenpm injected mice developed liver tumors. As an additional control for this experiment, sgRNA against 3 genes previously selected as candidate mTORC1 targets, *Arhegf2*, *Bat1*, and *Scl7a11*, were co-injected with c-MYC/ MCL1. However, none of them delayed c-MYC-driven HCC development, supporting the importance of targeting Cenpm to effectively blunt c-MYC-dependent hepatocarcinogenesis (Supplementary Fig. 19). To substantiate further the effective deletion of the *Cenpm* gene, we transfected sgCenpm lentivirus construct into HCC3-4 cells, a mouse HCC cell line with c-MYC activation. The TIDE assay result confirmed the effectiveness of our CRISPR/Cas9 system (Supplementary Fig. 20A). Consistent results were also found in the c-MYC/sg*Cenpm* liver tissues that were harvested at an early stage when c-MYC positive cells still existed (Supplementary Fig. 20B).

In summary, our study strongly suggests that CENPM is a critical downstream target of mTORC1 signaling in c-MYC HCC initiation.

Discussion

The present study systematically dissected the signaling pathways downstream of mTORC2/AKT1 in c-MYC-dependent hepatocarcinogenesis. The first key conclusion from our *in vivo* genetic investigation is that FOXOs, including FOXO1, the major FOXO family member in the liver, have limited relevance in regulating AKT1 signaling mediated c-MYC-driven HCC in mice. This finding contrasts with previous studies suggesting that AKT regulates liver physiology and pathophysiology by predominantly controlling FOXO1. For instance, it has been shown that liver-specific deletion of *Akt1* and *Akt2* in the liver led to glucose intolerance and insulin resistance. These defects could be normalized by co-deleting *Foxo1* in the liver (13). Loss of *Akt1/Akt2* led to liver regeneration defects. In *Akt1/Akt2/Foxo1* triple liver-specific KO mice, liver regeneration was restored, as seen in the wild-type mice (11). Similarly, mice with liver-specific deletion of *Akt1/Akt2* developed HCC over the long term. Liver tumor development could be abolished entirely in the *Akt1/Akt2/Foxo1* triple liver-specific KO mice (12). All these studies suggest that FOXO1 is a key molecule downstream of AKT signaling in the liver. In striking contrast to these data, our current study shows that loss of FOXO1 fails to restore c-MYC-driven HCC development in the absence of the mTORC2/AKT cascade. The results highlight that FOXO1 or FOXO family members may have distinct functions depending on different pathological stimuli. The present findings also indicate that suppressing FOXO family members may have limited value for treating c-MYC-dependent hepatocarcinogenesis.

Our current and previous studies demonstrate that TSC/mTORC1 cascade is necessary and sufficient for HCC development in c-MYC mice. The data also underline the critical role of the TSC complex in c-MYC-driven hepatocarcinogenesis. This conclusion is further supported by the fact that *TSC1/2* mutant human HCC samples were enriched in c-MYC activated tumors

(Supplementary Fig. 6). In mice, loss of TSC2 significantly accelerated c-MYC induced liver tumor formation (Supplementary Fig. 7). These results also support the possible use of mTOR inhibitors for HCC treatment. However, our RNASeq studies indicated that both MLN0128 and everolimus treatment downregulated genes were enriched in the apoptosis pathway (Figure 4). Specifically, several pro-apoptotic genes (*Bak1, Bcl10, Card19, Casp3, Ltbr, Noxa*) in these treatment groups were reduced compared with the vehicle group (Supplementary Fig. 21). Therefore, mTORC1 inhibitors might display even adverse effects on inducing apoptosis in the c-MYC/ MCL1 HCC model and in human corresponding tumors. Combining mTORC1 inhibitors with drugs targeting the apoptosis process may be needed for human HCC patients harboring c-Myc activation.

mTORC1 is known to function through the p70S6K/RPS6 and 4EBP1/eIF4E cascades. It is important to note that both p70S6K/RPS6 and 4EBP1/eIF4E cascades regulate protein translation as their primary functions. Nevertheless, eventually, the deregulated protein translation affects different targets. It has been established that p70S6K/RPS6 regulates tumor metabolism, such as *de novo* lipogenesis. Studies have shown that targeting the de-regulated metabolic pathway, such as deleting FASN, a major enzyme in *de novo* lipogenesis, could strongly delay c-MYC HCC development (27). However, the genes or pathways regulated by the 4EBP1/eIF4E cascade in HCC are not well-characterized. This is mainly because the 4EBP1/eIF4E cascade predominantly regulates protein translation, which is much more difficult to analyze technically. Here, we chose to use RNASeq in combination with everolimus or MLN0128 treatment of *c-MYC/ MCL1/Ricto^{KO}Tsc2^{KO}* mouse liver tumors to identify genes or pathways that are indirectly regulated by the 4EBP1/eIF4E cascade. Our study indicates that 4EBP1/eIF4E is the major signaling that modulates tumor cell proliferation and metabolic pathways directly contributing to tumor proliferation, such as PKM1 and LDHA/C (Supplementary Fig. 14B).

Finally, we identified CENPM as a downstream target of 4EBP1/eIF4E, as its expression was downregulated in c-MYC HCC by MLN0128, but not everolimus (Figure 6B and Supplementary Fig. 15A). Nonetheless, the regulation of CENPM by 4EBP1/eIF4E might be indirect. The eIF4E protein plays a crucial role in binding to the 5' cap structure of mRNA, and its availability often limits translation initiation. 4EBP1 binds to eIF4E and inhibits its function, thereby preventing translation initiation. Activation of the mTOR pathway leads to phosphorylation of 4EBP1, causing its dissociation from eIF4E and promoting translation initiation. Previous evidence indicates that the upregulation of CENPM promotes cancer progression through the mTOR signaling pathway (28). In addition, several microRNAs, including miR-214-3p (29), have been implicated in the post-transcriptional regulation of CENPM. Interestingly, miR-214-3p is also involved in regulating the 4EBP1 signaling (30). Therefore, the 4EBP1/eIF4E complex might regulate CENPM translation by interacting with microRNAs. However, the precise mechanisms underlying this regulation require further investigation. Furthermore, additional mechanisms might lead to the upregulation of CENPM in c-MYC driven HCC. Indeed, our bioinformatics analysis and experimental studies demonstrated that CENPM is also a direct transcriptional target of c-MYC. (Supplementary Figs. 22 and 23), supporting that c-MYC regulates CENPM via multiple mechanisms. Finally, we show that CENPM is an important mediator of c-MYC induced HCC. It is worth to note that it is unlikely that CENPM is the only key molecule in driving c-MYC induced HCC formation. Several other proteins, such as TAZ (17), SLC1A5 (16), etc., were also shown to be crucial for c-MYC driven hepatocarcinogenesis. Nevertheless, the current studies suggests that CENPM might be a valuable target for treating c-MYC driven HCC.

Materials and methods

Sex as a biological variable. Sex was not considered as a biological variable. Both male and females animals were used in this study.

Constructs and reagents

The plasmids used in the study, including pT3-elongation factor 1 alpha (EF1α)-myeloid cell leukemia 1 (MCL1), pT3-EF1α-c-MYC, pT3-EF1α-4EBP1A4, phosphorylated cytomegalovirus (pCMV)–cyclization recombination (Cre), and pCMV/sleeping beauty transposase (SB) have been described in our previous publications(25, 31). pT3-EF1α-FoxO1AAA plasmid was constructed from pCMV5-Myc-FoxO1AAA (#17547, Addgene, deposited by Dr. Domenico Accili at College of Physicians and Surgeons of Columbia University, New York). pT3-TTRpro-CreERT2 plasmid was constructed from pCAG-CreERT2 (#14797, Addgene, deposited by Dr. Connie Cepko at Harvard Medical School, Boston) using a standard molecular cloning approach. The pCMV4a-Flag-c-Myc construct was purchased from Addgene (#102625, Addgene, deposited by Dr. Hening Lin at Cornell University, New York). The pGL3 firefly luciferase reporter vector plasmid (Cat# E1751) and the pRL-CMV Renilla luciferase control reporter vector plasmid (Cat# E2231) were purchased from Promega (Madison, WI). To generate the pGL3-CENPM-promoter plasmid, a 2000bp DNA fragment of the human CNEPM promoter containing the predicted c-MYC binding site was cloned into the pGL3 vector. To generate the pGL3-Motif-Mut plasmid, a 1988bp truncated DNA fragment deleting the putative c-MYC binding site (CACCACGTGTTC) in the CENPM genome was cloned into the pGL3 vector.ForFor CRISPR-Cas9 mediated gene deletion, the sgRNA guide sequence was cloned into LentiCRISPRv2 puro (#98290, Addgene, deposited by Dr. Brett Stringer Lab at Griffith University, Brisbane) or PX330 (#42230, Addgene, deposited by Dr. Feng Zhang at Massachusetts Institute of Technology, Cambridge) according to the published protocol (32). The guide RNAs used in the study are listed in Supplementary Table 2. All plasmids were purified using the Endotoxin-free Maxi prep kit (Sigma-Aldrich, MO, USA). MLN0128 (I-3344) and everolimus (E-4040) were from LC Laboratories (Woburn, MA, USA), and tamoxifen was purchased from Sigma-Aldrich (St. Louis, MO, USA).

Hydrodynamic injection and mouse treatment

Wild-type *FVB/N* mice were obtained from Charles River Laboratories (Wilmington, MA, USA). *Tsc2*$^{fl/fl}$ mice (in C57BL/6J background), *Rictor*$^{fl/fl}$ mice (in C57BL/6J background), *Foxo1*$^{fl/fl}$ mice (in FVB/NJ background), and *Raptor*$^{fl/fl}$ mice (in C57BL/6J+N mixed background) were purchased from the Jackson Laboratory (Bar Harbor, ME, USA). *Rictor*$^{fl/fl}$*;Foxo1*$^{fl/fl}$ mice and *Rictor*$^{fl/fl}$;*Tsc2*$^{fl/fl}$ mice were generated by crossing *Rictor*$^{fl/fl}$ mice with *Tsc2*$^{fl/fl}$ mice or *Foxo1*$^{fl/fl}$ mice, respectively. The hydrodynamic tail vein injection was performed as described (33, 34). The plasmid mixture compounds, which induced mouse c-MYC/MCL1 HCC, are depicted in Supplementary Table 3. MLN0128 (I-3344) and everolimus (E-4040) were purchased from LC Laboratories (Woburn, MA, USA). MLN0128 was first dissolved in NMP (1-methyl-2-pyrrolidinone) (328634, Sigma-Aldrich) to make a stock solution of 20mg/ml, then 1:100 diluted into 15% PVP (81420 Sigma-Aldrich) /H2O. The diluted solution was stored at 4℃ in the dark before administration. Everolimus was dissolved in 100% ethanol to make a stock solution of 50 mg/ml and then mixed with 1%PBS to make a 0.2mg/ml working solution before administration. Tamoxifen (T5648, Sigma-Aldrich, MO, USA) was dissolved in corn oil for 1 hour in a roller (hybridization oven) at 65℃ to make a stock solution of 20mg/ml. Warm Tamoxifen at 65℃ for 10min before injecting.

MLN0128 (1mg/kg/day), everolimus (1mg/kg/day) or vehicle was orally administered via gavage for 3 weeks (6 days a week) starting 6 days after plasmid injection, respectively. Mice were sacrificed 3.7 weeks after hydrodynamic injection (3 weeks after treatment). Two weeks post-injection of c-MYC/MCL1/TTR-CreERT2 plasmids (when tumor nodules are visible on the liver surface), a group of mice was harvested as a pretreatment cohort, and additional mice were either intraperitoneally injected with corn oil or tamoxifen (9mg/40g body weight), 3 times, one every other day. Tamoxifen administration allows the activation of the Cre recombinase and the subsequent deletion of Raptor only in TTR promoter (+) HCC tumor cells. Mice were housed and monitored according to protocols approved by the committee for animal research at the University

of California, San Francisco (Protocol number AN185770) and the University of Hawaii Cancer Center. The abdominal girth and the signs of morbidity or discomfort were monitored for all mice.

Cell lines, cell culture, and *in vitro* experiments

Three human HCC cell lines (SNU449, HLE, and HLF) were used in this study. The cell lines were obtained from the American Type Culture Collection (ATCC, Manassas, VA, USA). All cells were authenticated and tested clear of mycoplasma contamination. SNU449 cells were cultured in Roswell Park Memorial Institute 1640 medium (RPMI-1640), while HLE and HLF cells were cultured in Dulbecco's modified Eagle medium (DMEM) with 10% fetal bovine serum (FBS) at 37°C in 5% CO2 (v/v) humidified incubator.

For lentiviral transduction, a 6-well plate of 50% confluent HEK293FT cells were transfected in OptiMEM with 5ul Lipofectamine 2000 reagents (Invitrogen), 2μg packaging plasmids (equal volumes of pVSV-G, pMDL, and pRSV) and 2μg lentivirus. 48 hours later, the viral supernatant was harvested and filtered through a 0.45 μm filter (Millipore). For lentivirus transfection, cells were seeded into 6-well plates. The viral supernatant was added to culture media at an equal volume. After 24 hours, the culture media was supplemented with 2μg/ml concentrations of puromycin for selection.

For colony-formation assay, cells transfected with pLenti-puro-sgCENPM/EGFP lentivirus were plated in 6-well culture plates at a density of 500 cells per well, respectively, in triplicate. Colonies were stained with crystal violet two weeks later and then counted for quantification.

For knockdown studies, cells were transfected with scramble small interfering RNA (siRNA) or siRNA directed against the human *CENPM* gene (stB003419, RiboBio, Guangzhou, China), according to the manufacturer's recommendations. After incubating for 48 hours, cell proliferation was assessed using the EdU Cell Proliferation kit (Thermo Fisher Scientific, MA, USA). Experiments were repeated at least three times in triplicate.

Analysis of chromosome segregation during mitosis

CENPM knockout (sg*CENPM*) and control (sg*EGFP*) HLF cells were used. To synchronize the cells in the G0/G1 phase, they were incubated in DMEM/F12 growth media containing 0.1% FBS for 24 hours, ensuring a maximum number of cells in the G0/G1 phase (35). The cells were then incubated in DMEM with 10% FBS for 24h at 37 °C and 5% CO_2. After incubation, the cells were washed with PBS, fixed with ice-cold methanol, permeabilized with 0.1% Triton X-100, and blocked with 0.1% Triton X-100 and 10% normal goat serum in PBS. They were then incubated overnight at 4°C with antibodies against acetylated α-tubulin (1:200, Sigma-Aldrich) and γ-tubulin (1:500, Sigma-Aldrich), followed by a 1-hour incubation with fluorescent secondary antibodies (1:200). Nuclei were stained with DAPI (Prolong Gold w/DAPI, Invitrogen), and chromosomal lagging or mis-segregation was analyzed using confocal microscopy.

Histology and immunohistochemistry (IHC)

Mouse liver tissues were fixed in 4% paraformaldehyde overnight, embedded in paraffin, and sectioned as described previously (15, 36). For immunohistochemistry, the sections were incubated with the primary antibodies overnight at 4°C. The immunoreactivity was visualized with the Vectastain ABC Elite Kit (Vector Laboratories Inc.) and DAB (Vector Laboratories, Inc.). Slides were then counterstained with hematoxylin. The primary antibodies used in the present investigation are listed in Supplementary Table 4. Quantification was performed using the ImageJ 1.8.0 software (National Institutes of Health, USA, https://imagej.nih.gov/ij/download.html).

Protein extraction and Western blot analysis

Frozen mouse liver tumors were homogenized, and cultured cell samples were lysed in Mammalian Protein Extraction Reagent (Thermo Fisher Scientific, MA, USA) containing the

Complete Protease Inhibitor Cocktail (Thermo Fisher Scientific). Protein concentrations were determined with the Bio-Rad Protein Assay Kit (Bio-Rad, CA, USA). The lysates were denatured by boiling in 2×Laemmli sample buffer (1610737, Bio-Rad). Aliquots of 30 μg protein lysates were separated by SDS-PAGE (M00654, GenScript, NJ, USA) and then transferred onto PVDF membranes (Bio-Rad). Membranes were blocked in 10% non-fat milk in Tris-buffered saline containing 0.05% Tween-20 and incubated with primary antibodies at 4°C overnight. Then membranes were incubated with horseradish peroxidase-secondary antibody (Jackson ImmunoResearch Laboratories Inc., PA, USA) for 1 hour at room temperature and developed with ClarityTM Western ECL Substrate (170-5061, Bio-Rad). The primary antibodies used in the present investigation are listed in Supplementary Table 5.

RNA extraction, reverse transcription, and real-time PCR

Total RNA was extracted from frozen mouse liver specimens and cultured cell samples using the Quick-RNA™ Miniprep Kit (R1055, Zymo Research, Irvine, CA, USA). cDNA was generated using the iScript™ Reverse Transcription Supermix (1708841, Bio-Rad Laboratories, Hercules, CA, USA), according to the manufacturer's instructions. mRNA expression was determined by qPCR using the iTaq™ Universal SYBR® Green Supermix (1725124, Bio-Rad Laboratories, Hercules, CA, USA) in the QuantStudio™ 6 Flex system (Applied Biosystems). The expression of each specific gene mRNA was normalized with the 18S rRNA. Thermal cycling conditions included an initial hold period at 95°C for 10 min, which was followed by a three-step PCR program of 95°C for 15 sec, 60°C for 1 min, and 72°C for 30 sec for a total of 40 cycles. Primers used in this study are shown in Supplementary Table 6.

RNA sequencing analysis

To analyze the role of FOXOs during c-MYC induced hepatocarcinogenesis, total RNA was

extracted from mouse injected with c-MYC/pT3 (n=3), c-MYC/FOXO1AAA (n=3) as well as *FVB/N* wild-type normal livers (n=4) using the Quick-RNA Miniprep Kit (Zymo Research, CA,USA). To analyze downstream target genes of p70S6K/RPS6 and 4EBP1/eIF4E, total RNA was extracted from mouse *c-MYC/MCL1/Rictor^{KO}Tsc2^{KO}* HCCs treated with MLN0128 (n=3), everolimus (n=3), vehicle (n=3) as well as C57BL/6 wild-type normal livers (n=3) using the Quick-RNA Miniprep Kit (Zymo Research, CA, USA). Experimental design had 4 groups:“MLN”; (MLN0128), “EVE” (everolimus), “VEH” (vehicle), and “NL” (normal liver). The RNA quality control was determined using Agilent RNA 6000 Nano Kit (Agilent Technologies, CA, USA) and Bioanalyzer (Agilent Technologies, CA, UAS). Novogene (Sacramento, CA, USA) performed library preparation and sequencing. All analyses were performed in R. Experimental design had 4 groups: "MLN" (MLN0128), "EVE" (everolimus), "VEH" (vehicle), and "NL" (normal liver). Gene read counts were in Ensembl Gene ID and converted to Entrez Gene ID. Corresponding Symbol annotations and full gene names were added using the "org.Mm.eg.db" library. The R package "edgeR" and glmTreat function were used to identify differentially expressed genes (DEGs). DEGs were limited by a p-value of 0.05 and an FDR (False Discovery Rate) of 0.05. The Venn diagram was drawn using the VennDiagram package. KEGG pathway enrichment analysis were performed using ggplot2 package. The RNAseq data for this study were deposited in the Gene Expression Omnibus database (GSE275889, GSE276215).

Chromatin Immunoprecipitation (ChIP) Assay

SNU449 cells were transfected with pCMV4a-Flag-c-Myc using Lipofectamine 3000 (Invitrogen, L3000001) and CHIP was performed using the Zymo-Spin ChIP Kit following the manufacturer's instructions (Cat# D5209, Zymo Research). Briefly, 15 µL of Lipofectamine 3000 was diluted in 250 µL of Opti-MEM and incubated at room temperature for 5 minutes. Separately, 10 µg of plasmids and 20 µL of P3000 were mixed in 250 µL of Opti-MEM. After 5 minutes, the two mixtures

were combined and incubated for an additional 20 minutes at room temperature. This DNA-lipid complex and $2.5x10^6$ cells were then added to the cell culture plate. After 48 hours of transfection, the cells were harvested. DNA and protein in the cell samples were crosslinked with 1% formaldehyde, followed by sonication (30 s "ON", 30 s "OFF" for 12 cycles) on ice. Immunoprecipitation was performed using a Flag-tag antibody (Proteintech, 66008-4-Ig) overnight at 4°C, with rabbit anti-IgG (CST, #2729, 1:1000) as a negative control. DNA-protein complexes were pulled down using protein A magnetic beads and reverse-crosslinked to release the DNA. The purified DNA was used as a template for PCR. Input samples served as positive controls. PCR cycling conditions were: 10 minutes at 98°C, followed by 35 cycles of 10 seconds at 98°C, 5 seconds at 55°C, and 20 seconds at 72°C. PCR products were then run on a DNA gel to visualize the target bands. The primers specific for *CENPM* promoter region are: *CENPM*-ChIP forward: 5'- gaatgaaagtgaacaaaggaat -3'; *CENPM*-ChIP reverse: 5'- cctcttaaaggaaccgaacc -3'.

CUT & RUN assay

The CUT & RUN assay was conducted following the manufacturer's protocol (Vazyme, HD101). Briefly, SNU449 cells were rinsed with PBS and incubated with ConA Beads Pro at room temperature for 10 minutes. c-Myc/N-Myc antibody (1:50, Cell Signaling Technology, 13987S) was added and incubated at 4°C overnight. IgG (1:50, Cell Signaling Technology, 2729S) was used as a negative control. The samples were then washed twice, followed by the addition of pG-MNase Enzyme and incubation at 4°C for 1 hour. After washing twice, CaCl2 was added, and the samples were incubated for 1.5 hours on ice. Stop buffer was then added, and the samples were incubated at 37°C for 30 minutes. Finally, DNA was extracted and quantified by qPCR. The primers specific for *CENPM* promoter region are: *CENPM*-ChIP forward: 5'- gaatgaaagtgaacaaaggaat -3'; *CENPM*-ChIP reverse: 5'- cctcttaaaggaaccgaacc -3'.

Dual-luciferase reporter assay

The pCMV4a-Flag-c-Myc transfected SNU449 human HCC cells were plated in triplicate in 24-well plates at 70-80% confluency. Plasmids were transfected using the Lipofectamine 2000 reagents (Invitrogen). In brief, cells were transfected with 600ng of pLG3-*CENPM*-promoter plasmids or pGL3-Motif-Mut plasmids. The pGL3 empty vector plasmid was applied as a control. Meanwhile, HCC cells in each group were also transfected with 16ng of pRL-CMV plasmids. Cells were harvested 48 hours post-transfection. According to the manufacturer's protocol, we assessed the luciferase activity using the Dual-Luciferase® Reporter Assay System (Promega, Cat#1910). The Synergy^{TM} HT microplate read firefly and Renilla luciferase. Normalization to *Renilla* luciferase was performed in all samples. Experiments were repeated at least three times in triplicates.

Retrieval and analysis on the TCGA human HCC data

To investigate the relationship between MYC activation and *TSC* mutation status in human HCC samples, the TGCA data sets were retrieved based on the cBioPortal for Cancer Genomics (http://www.cbioportal.org). The overall sample size is 374 HCCs from the TCGA-LIHC database. The mutation data was extracted from the cBioPortal for Cancer Genomics. The data was analyzed and visualized in R using multiple packages. For MYC activation status, we extracted expression data of 30 well-characterized c-MYC target genes based on the TCGA-LIHC database. In order to reflect the c-MYC activation trends, all these 30 c-MYC target genes expression level were used for clustering analysis of transcription abundance. All genes were clustered into three expression profiles (MYC-high, MYC-low and MYC-medium) using the K-means clustering method. The data objects with similar characteristics of c-MYC activation would be grouped into the same clusters. Heatmap were generated using the pheatmap package in R.

641 **Statistical analysis**

642 The Prism 7.0 software (GraphPad, San Diego, CA, USA) was used to analyze the data. The data
643 were presented as means ± SD. Statistical analyses were conducted using Student's t-test, Chi-
644 square test and One-way ANOVA test. Survival curves were estimated using the Kaplan-Meier
645 method and compared using the log-rank test. *P*-value <0.05 was considered statistically
646 significant.

647

648 **Study approval:** All mouse experiments were performed in accordance with protocols approved
649 by Institutional Animal Care Use Committee (IACUC) at University of California, San Francisco
650 (Protocol number AN185770) and the University of Hawaii Cancer Center.

651

652 **Data availability:** All datasets generated and analyzed for this current study are available from
653 the corresponding author on reasonable request.

654

655 **Author contributions**

656 S.L, H.W. and X.C. performed study concept and design; Y.Z., S.Z., G.Q., X.W., A.Y.,J.W., Z.X.,
657 M.E., and G.C. performed the experiments. Y.Z., S.Z. and H.W. drafted the manuscript; J.C., N.C.
658 and M.X. provided technical and material support; X.W., H.X. and S.D. performed data analysis
659 and interpretation of the sequencing data; S.L, D.F.C., X.C., X.W., Y.D., X.S., A.Y., and H.W.
660 performed review and revision of the paper. All authors read and approved the final paper.

661

662 **Conflict of interest statement:** The authors declare no potential conflicts of interest.

663

664 **Financial support statement:** This study is supported by NSFC under Grants 82372660 to HW;
665 NIH under Grants R01CA239251 and R01CA250227 to XC; P30DK026743 to UCSF Liver Center;

666 U54GM138062, P20GM103466, U54MD007601, U54HG013243 and P20GM139753 to YD.
667 Sichuan Science and Technology Program 2024NSFC0058 to SZ. 1·3·5 project Clinical Research
668 Fund 2024HXFH030 to SZ. Natural Science Basic Research Program of Shaanxi 2024JC-YBQN-
669 0832 to YZ.

670

References

1. Bray F, et al. Global cancer statistics 2018: GLOBOCAN estimates of incidence and mortality worldwide for 36 cancers in 185 countries. *CA Cancer J Clin.* 2018;68(6):394-424.
2. EASL Clinical Practice Guidelines: Management of hepatocellular carcinoma. *J Hepatol.* 2018;69(1):182-236.
3. Llovet JM, et al. Sorafenib in advanced hepatocellular carcinoma. *N Engl J Med.* 2008;359(4):378-90.
4. Cheng AL, et al. Efficacy and safety of sorafenib in patients in the Asia-Pacific region with advanced hepatocellular carcinoma: a phase III randomised, double-blind, placebo-controlled trial. *Lancet Oncol.* 2009;10(1):25-34.
5. Llovet JM, et al. Immunotherapies for hepatocellular carcinoma. *Nat Rev Clin Oncol.* 2022;19(3):151-72.
6. Sangro B, et al. Exposure-response analysis for nivolumab plus ipilimumab combination therapy in patients with advanced hepatocellular carcinoma (CheckMate 040). *Clin Transl Sci.* 2023.
7. Lu X, et al. Role of the Mammalian Target of Rapamycin Pathway in Liver Cancer: From Molecular Genetics to Targeted Therapies. *Hepatology.* 2021;73 Suppl 1(Suppl 1):49-61.
8. Hara K, et al. Raptor, a binding partner of target of rapamycin (TOR), mediates TOR action. *Cell.* 2002;110(2):177-89.
9. Sarbassov DD, et al. Rictor, a novel binding partner of mTOR, defines a rapamycin-insensitive and raptor-independent pathway that regulates the cytoskeleton. *Curr Biol.* 2004;14(14):1296-302.
10. Zhou Y, et al. Mammalian Target of Rapamycin Complex 2 Signaling Is Required for Liver Regeneration in a Cholestatic Liver Injury Murine Model. *Am J Pathol.* 2020;190(7):1414-26.
11. Pauta M, et al. Akt-mediated foxo1 inhibition is required for liver regeneration. *Hepatology.* 2016;63(5):1660-74.
12. Wang Q, et al. Spontaneous Hepatocellular Carcinoma after the Combined Deletion of Akt Isoforms. *Cancer Cell.* 2016;29(4):523-35.
13. Lu M, et al. Insulin regulates liver metabolism in vivo in the absence of hepatic Akt and Foxo1. *Nat Med.* 2012;18(3):388-95.
14. Stine ZE, et al. MYC, Metabolism, and Cancer. *Cancer Discov.* 2015;5(10):1024-39.
15. Xu Z, et al. The mTORC2-Akt1 Cascade Is Crucial for c-Myc to Promote Hepatocarcinogenesis in Mice and Humans. *Hepatology.* 2019;70(5):1600-13.
16. Liu P, et al. A functional mammalian target of rapamycin complex 1 signaling is indispensable for c-Myc-driven hepatocarcinogenesis. *Hepatology.* 2017;66(1):167-81.
17. Wang H, et al. TAZ is indispensable for c-MYC-induced hepatocarcinogenesis. *J Hepatol.* 2022;76(1):123-34.
18. Judge SM, et al. Genome-wide identification of FoxO-dependent gene networks in skeletal muscle during C26 cancer cachexia. *BMC Cancer.* 2014;14:997.
19. Yang L, et al. Integrative Transcriptome Analyses of Metabolic Responses in Mice Define Pivotal LncRNA Metabolic Regulators. *Cell Metab.* 2016;24(4):627-39.
20. Liang CQ, et al. FoxO3 restricts liver regeneration by suppressing the proliferation of hepatocytes. *NPJ Regen Med.* 2022;7(1):33.
21. Inoki K, et al. TSC2 is phosphorylated and inhibited by Akt and suppresses mTOR signalling. *Nat Cell Biol.* 2002;4(9):648-57.
22. Shaw RJ, and Cantley LC. Ras, PI(3)K and mTOR signalling controls tumour cell growth. *Nature.* 2006;441(7092):424-30.

23. Cancer Genome Atlas Research Network. Electronic address wbe, and Cancer Genome Atlas Research N. Comprehensive and Integrative Genomic Characterization of Hepatocellular Carcinoma. *Cell.* 2017;169(7):1327-41 e23.
24. Liang B, et al. Differential requirement of Hippo cascade during CTNNB1 or AXIN1 mutation-driven hepatocarcinogenesis. *Hepatology.* 2023;77(6):1929-42.
25. Wang C, et al. 4EBP1/eIF4E and p70S6K/RPS6 axes play critical and distinct roles in hepatocarcinogenesis driven by AKT and N-Ras proto-oncogenes in mice. *Hepatology.* 2015;61(1):200-13.
26. Xie X, et al. Ribosomal proteins: insight into molecular roles and functions in hepatocellular carcinoma. *Oncogene.* 2018;37(3):277-85.
27. Wang H, et al. Therapeutic efficacy of FASN inhibition in preclinical models of HCC. *Hepatology.* 2022;76(4):951-66.
28. Liu C, et al. Upregulation of CENPM facilitates lung adenocarcinoma progression via PI3K/AKT/mTOR signaling pathway. *Acta Biochim Biophys Sin (Shanghai).* 2022;54(1):99-112.
29. Zou Y, et al. LncRNA HCG18 contributes to the progression of hepatocellular carcinoma via miR-214-3p/CENPM axis. *J Biochem.* 2020;168(5):535-46.
30. Das F, et al. MicroRNA-214 Reduces Insulin-like Growth Factor-1 (IGF-1) Receptor Expression and Downstream mTORC1 Signaling in Renal Carcinoma Cells. *J Biol Chem.* 2016;291(28):14662-76.
31. Shachaf CM, et al. MYC inactivation uncovers pluripotent differentiation and tumour dormancy in hepatocellular cancer. *Nature.* 2004;431(7012):1112-7.
32. Sanjana NE, et al. Improved vectors and genome-wide libraries for CRISPR screening. *Nat Methods.* 2014;11(8):783-4.
33. Carlson CM, et al. Somatic integration of an oncogene-harboring Sleeping Beauty transposon models liver tumor development in the mouse. *Proc Natl Acad Sci U S A.* 2005;102(47):17059-64.
34. Chen X, and Calvisi DF. Hydrodynamic transfection for generation of novel mouse models for liver cancer research. *The American journal of pathology.* 2014;184(4):912-23.
35. Varadkar P, et al. Live Cell Imaging of Chromosome Segregation During Mitosis. *J Vis Exp.* 2018(133).
36. Shang R, et al. Cabozantinib-based combination therapy for the treatment of hepatocellular carcinoma. *Gut.* 2020.

Figure Legends

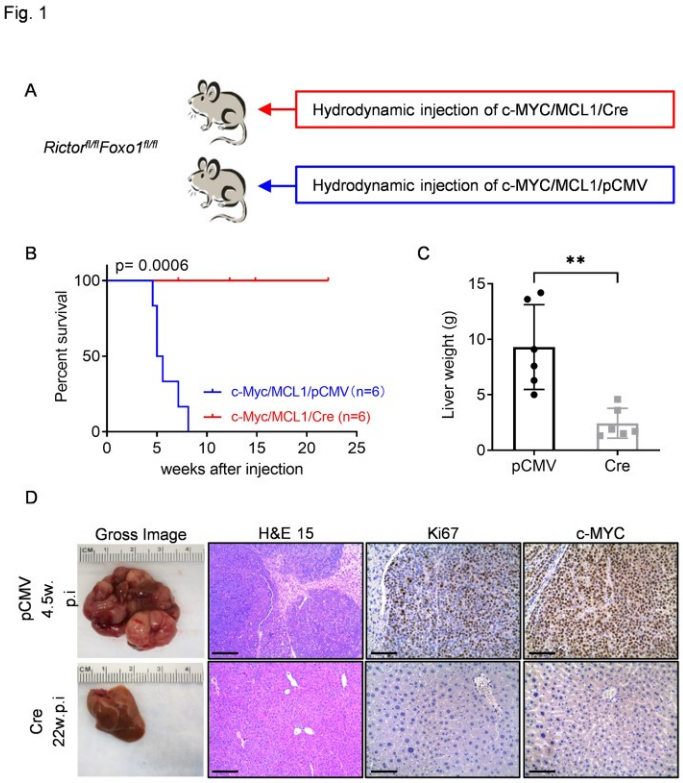

Figure 1. *FoxO1* deletion fails to rescue the loss of mTORC2's tumor inhibitory effects. (A) Study design. *Rictor*$^{fl/fl}$*Foxo1*$^{fl/fl}$ conditional knockout mice were hydrodynamically injected with plasmid mixtures of c-MYC/ MCL1 and Cre recombinase in pCMV backbone (c-MYC/ MCL1/Cre, n = 6). The control mice were hydrodynamically injected with c-MYC/MCL1 and pCMV empty vector (c-MYC/MCL1/pCMV, n = 6) constructs. Mice were monitored for tumor development and were euthanized when moribund tumors developed or till the end of the observation period. **(B)** Survival curve of mice in both groups. The Kaplan-Meier comparison was performed, p = 0.0006. **(C)** Comparison of liver weight between the two groups. Data are presented as mean ± SD. Student's t-test. **, p<0.01. **(D)** Representative images of macroscopy pictures of the liver, H&E stainings, and immunohistochemical stainingof Ki67 and c-MYC. Scale bars: 200μm for H&E, 100μm for Ki67 and c-MYC.

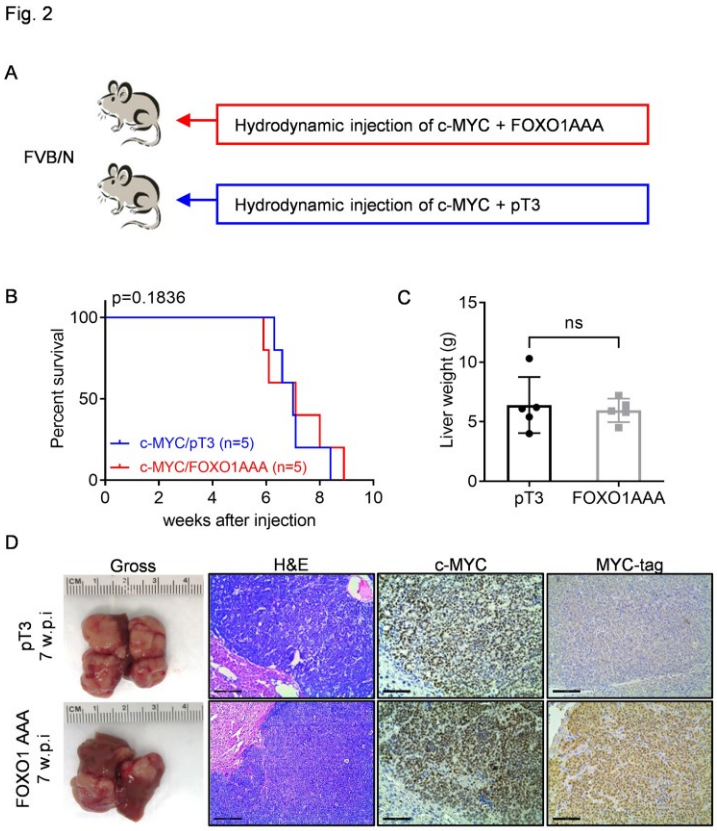

Figure 2. Lack of effect of FOXO1 activation on c-MYC-induced hepatocarcinogenesis. (A) Study design. *FVB/N* mice were hydrodynamically injected with plasmid mixtures of c-MYC and a constitutively active mutant of FoxO1 (FoxO1AAA) in pT3-EF1α backbone with MYC-tag (c-MYC/FoxO1AAA, n = 5). The control mice were hydrodynamically injected with c-MYC/MCL1 and pT3-EF1α empty vector (c-MYC/pT3, n = 5). Mice were monitored for tumor development and were euthanized when moribund tumors developed or till the end of the observation period. **(B)** Survival curve of mice in both groups. The Kaplan-Meier comparison was performed, $p = 0.1836$. **(C)** Comparison of liver weight between the two groups. Data are presented as mean ± SD. Student's t-test. ns, no significant. **(D)** Representative images of macroscopy pictures of the liver. H&E stainings, and immunohistochemical stainingof c-MYC and MYC-tag. Scale bars: 200μm for H&E, 100μm for c-MYC and MYC-tag.

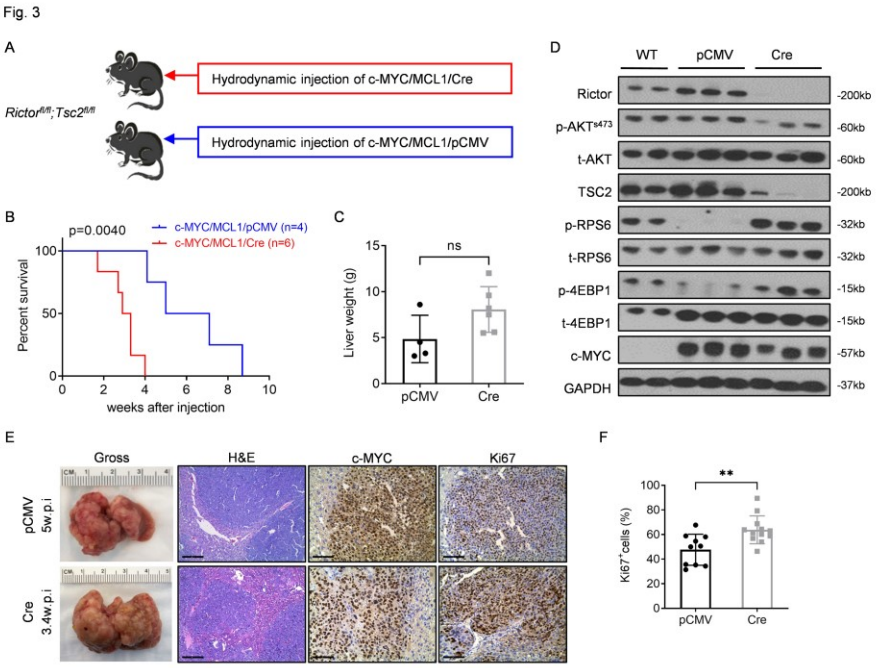

Figure 3. Compensation of mTORC2's tumor inhibitory effects by *Tsc2* deletion. (A) Study design. *Rictor*$^{fl/fl}$*Tsc2*$^{fl/fl}$ conditional knockout mice were hydrodynamically injected with plasmid mixtures of c-MYC/MCL1 and Cre recombinase in pCMV backbone (c-MYC/MCL1/Cre, n = 4). The control mice were hydrodynamically injected with c-MYC/MCL1 and pCMV empty vector (c-MYC/ MCL1/pCMV, n = 6). Mice were monitored for tumor development and were euthanized when moribund tumors developed or till the end of the observation period. **(B)** Survival curve of mice in both groups. The Kaplan-Meier comparison was performed, p = 0.0040. **(C)** Comparison of liver weight between the two groups. Data are presented as mean ± SD. Student's t-test. ns, no significant. **(D)** Western blot results show the expression of Rictor, TSC2, and other proteins in the mTORC2/AKT cascades. Abbreviations: WT, wild-type. **(E)** Representative images of macroscopy pictures of the liver, H&E stainings, and immunohistochemical stainingof Ki67 and c-MYC. Scale bars: 200μm for H&E, 100μm for Ki67 and c-MYC. **(F)** Quantification results of percentage of Ki67 positive cells in the two groups. Data are presented as mean ± SD. Student's t-test. **, p<0.01.

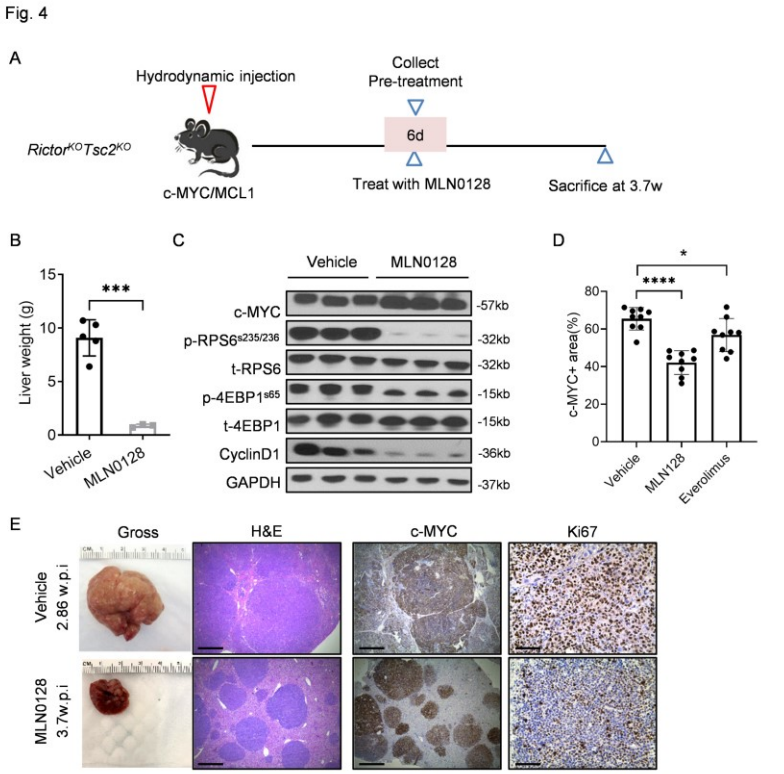

Figure 4. Inhibition of c-MYC/MCL1/*Rictor*^{KO}*Tsc2*^{KO} tumor growth by MLN0128 treatment. **(A)** Study design. The c-MYC/MCL1/*Rictor*^{KO}*Tsc2*^{KO} murine tumor model was established by hydrodynamic injection. At 6 days post-injection, one group of mice (n = 3) was sacrificed, and mouse livers were harvested for analysis as the pre-treatment group. The remaining mice were treated with MLN0128 (n = 3) or vehicle (n = 5) for 3 weeks. Subsequently, all mice were sacrificed for analysis. **(B)** Comparison of liver weight between the MLN0128 and the vehicle-treated groups. Data are presented as mean ± SD. Student's t-test. ***, $p<0.001$. **(C)** Western blot analysis showing levels of c-MYC, Cyclin D1, and key molecules downstream of mTORC2 (n = 3, 3). GAPDH was used as the loading control. **(D)** Comparison of c-MYC positive areas in the MLN0128, Everolimus and vehicle-treated groups. **(E)** Representative images of gross views of the liver, H&E stainings, and immunohistochemical stainingof Ki67 and c-MYC. Scale bars: 500μm for H&E and c-MYC, 100μm for Ki67. Data are presented as mean ± SD. Student's t-test. *, $p<0.05$. ****, $p<0.0001$.

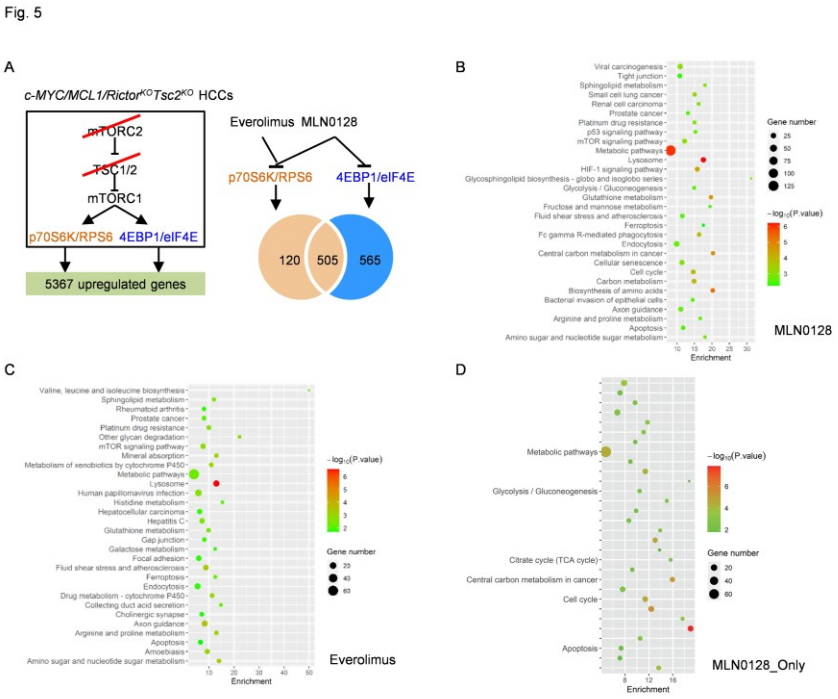

Figure 5. Analysis of p70S6K/RPS6 and 4EBP1/eIF4E downstream target genes. (A) Study design. Schematic diagram showing the signaling pathways involved in the c-MYC/MCL1/*Rictor*^{KO}*Tsc2*^{KO} tumors (left panel). RNAseq was performed on the normal liver tissue and c-MYC/MCL1/*Rictor*^{KO}*Tsc2*^{KO} tumors treated with vehicle, everolimus, or MLN0128 (n = 3, 3, 3). The Venn diagram shows the number of differentially expressed genes (DEGs). **(B)** KEGG analysis of the DEGs downregulated by MLN0128. **(C)** KEGG analysis of the DEGs downregulated by everolimus. **(D)** KEGG analysis of the DEGs downregulated by MLN0128, but not by everolimus.

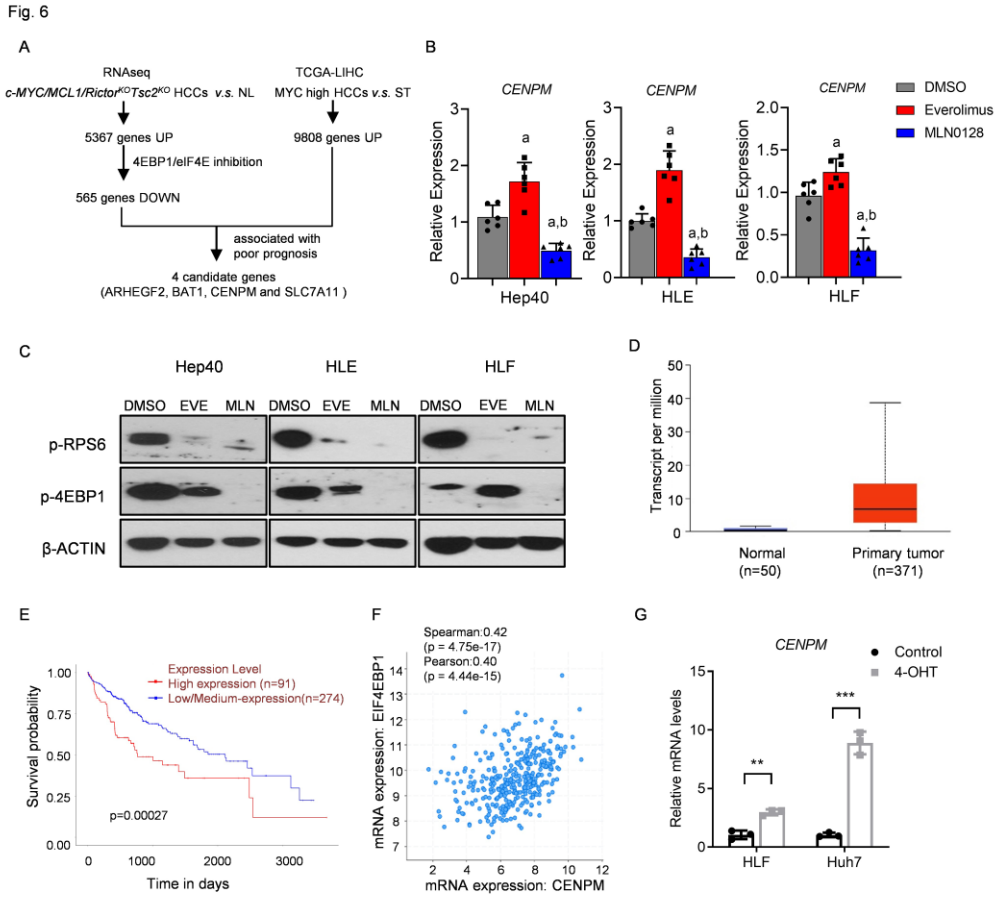

811

812 **Figure 6. CENPM is a central effector downstream of 4EBP1/eIF4E signaling in c-MYC**
813 **HCCs. (A)** Schematic diagram illustrating the identification of target genes regulated by
814 4EBP1/eIF4E signaling in c-MYC HCCs. **(B)** qPCR results showing *CENPM* mRNA levels in the
815 three HCC cell lines (Hep40, HLE, and HLF) treated with DMSO, everolimus, and MLN0128 (n =
816 6, 6, 6). Data are presented as mean ± SD. Tukey–Kramer test. At least p<0.05. a, versus DMSO;
817 b, versus Everolimus. **(C)** Western blot analysis depicting the levels of p-RPS6 and p-4EBP1 in
818 HCC cells treated with DMSO and MLN0128. β-Actin was used as the loading control. **(D)**
819 Expression of CENPM in the human HCC samples and normal liver based on the TCGA-LIHC
820 dataset. Data are presented as mean ± SD. Student's t-test. *p*<1E-12. **(E)** Survival curve of the
821 HCC patients with high *CENPM* expression compared to those with low/medium *CENPM*
822 expression (from https://ualcan.path.uab.edu/ website). Samples were categorized into two

groups: High expression (with TPM values above upper quartile) and Low/Medium expression (with TPM values below upper quartile). The Kaplan-Meier comparison was performed, p = 0.00027. **(F)** Correlation between *CENPM* and *EIF4EBP1* mRNA levels in human HCCs. **(G)** qPCR results showing *CENPM* mRNA levels in the MYC-ER transfected HCC cell lines (Hep40 and HLE) after treatment of DMSO or 4-hydro tamoxifen (4-OHT) (n = 3, 3). Data are presented as mean ± SD. Student's t-test. **, p<0.01. ***, p<0.001.

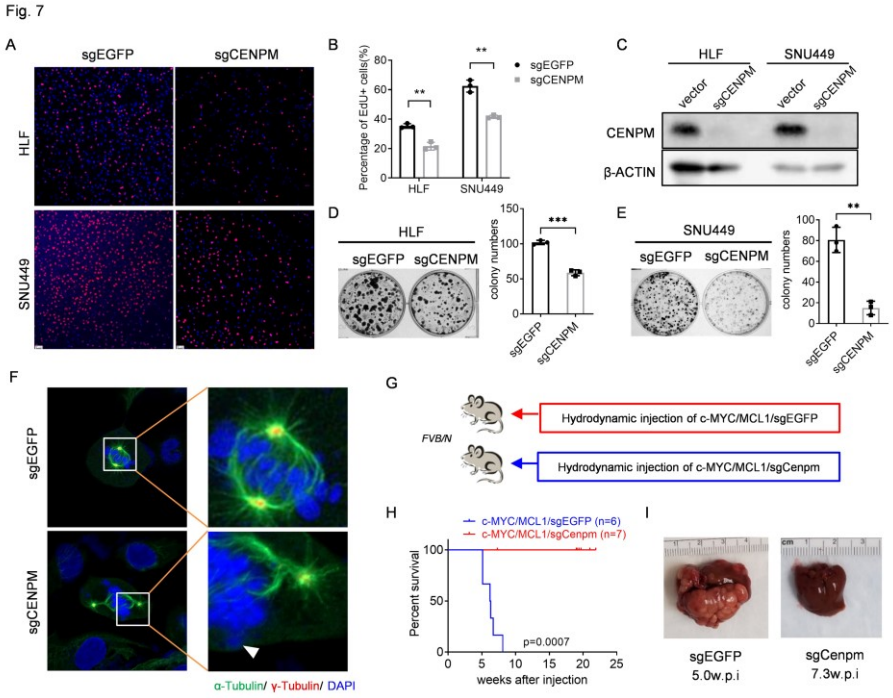

Figure 7. Targeting CENPM suppresses HCC cell proliferation and c-MYC-induced hepatocarcinogenesis. (A, B) Representative images (A) and quantification (B) of EdU staining in HLF and SNU449 cells transfected with sgEGFP or sgCENPM (n = 3, 3). Data are presented as mean ± SD. Student's t-test. **, p<0.01. **(C)** Western blot analysis confirming the knockout of CENPM in the HCC cells. β-Actin was used as the loading control. **(D, E)** Representative images and quantification of colony formation assay in the sgEGFP or sgCENPM transfected HLF (D) and SNU449 (E) cells. Data are presented as mean ± SD. Student's t-test. **, p<0.01. ***, p<0.001.

838 **(F)** Representative images of immunofluorescence staining of α-tubulin (indicating microtubule,
839 kinetochore or spindle fibers), γ-tubulin (centrosome), and DAPI (indicating chromosomes) in the
840 CENPM KO cells and the control cells during mitosis. Lagging chromosomes (indicated by white
841 triangle) or mis-segregation were observed in almost all the CENPM KO cells. **(G)** Study design.
842 *FVB/N* mice were hydrodynamically injected with plasmid mixtures of c-MYC/MCL1 and CRISPR
843 plasmid with gRNA targeting mouse *Cenpm* genome (c-MYC/MCL1/sgCenpm, n = 7). The control
844 mice were hydrodynamically injected with c-MYC/MCL1 and sgEGFP (c-MYC/MCL1/sgEGFP, n
845 = 6). Mice were monitored for tumor development and were euthanized when moribund tumors
846 developed or till the end of the observation period. **(H)** Survival curve of mice in both groups. The
847 Kaplan-Meier comparison was performed, $p = 0.0007$. **(I)** Representative images of macroscopy
848 pictures of the liver in both groups.